Electron energy loss in multilayered slabs. III. Anisotropic media

1995 J. Phys.: Condens. Matter 7 3405

(http://iopscience.iop.org/0953-8984/7/18/005)

J. Phys.: Condens. Matter 7 (1995) 3405–3419. Printed in the UK

Electron energy loss in multilayered slabs: III. Anisotropic media

J P R Bolton and M Chen

Physics Department, The Open University, Walton Hall, Milton Keynes MK7 6AA, UK

Received 10 August 1994

Abstract. This work extends the non-retarded semiclassical dielectric theory of electron energy loss to multilayers composed of anisotropic media. A transfer matrix recurrence relation is used to obtain expressions for the potential, dispersion relation and energy-loss spectrum, valid for any finite number of anisotropic layers and any orientation of the anisotropy axes. Both normal and parallel incidence are considered in the non-retarded limit. These theoretical results are illustrated by application to graphite surfaces and graphite–diamond interfaces.

1. Introduction

The study of electron energy loss in anisotropic solids has a long history [1]. Energy loss measurements on graphite [2, 3, 4] and the CuO-based high-temperature superconductors [5, 6] have shown that the detailed structure of the loss spectrum depends on the relative orientation of the beam direction and the anisotropy axes. Various authors have addressed the task of extending dielectric theory to anisotropic media, but the algebra is cumbersome and theoretical analysis has been confined to bulk media in the non-retarded limit [1, 7, 8, 9]. The theory has therefore reached to the same stage of development as Hubbard's work on isotropic loss spectra, before the work of Ritchie on normal incidence through slabs [10] or that of Howie on parallel incidence near interfaces [11].

In two recent papers (referred to here as papers I and II) we have developed the retarded dielectric theory of electron energy loss in *isotropic* multilayered slabs. Paper I dealt with normal incidence [12], while the paper II dealt with parallel incidence [13]. Starting from transfer matrix recurrence relations and using computer algebra as a guide, we obtained compact formulae for the Hertz vector, the dispersion relation and the energy-loss spectrum, valid for any number of isotropic layers.

Our primary goal in this paper is to derive formulae, analogous to those of Ritchie and Howie, but valid for single anisotropic slabs and single interfaces between anisotropic media. It turns out that techniques developed in papers I and II for multilayered isotropic slabs can be carried over completely to the anisotropic non-retarded case. We will therefore develop formulae that are valid for any number of anisotropic layers, with the anisotropy axes in arbitrary orientations and the electron beam travelling either normal or parallel to the interfaces. Formulae for single slabs and interfaces will then emerge as special cases of these more general results.

The geometry under consideration can be specified as follows. An n-layered stratified slab extends to infinity in the x- and y-directions and from $z = 0$ to $z = a$. The slab and its surroundings define $n + 2$ separate regions. The internal regions of the slab are labelled

0953-8984/95/183405+15$19.50

1, ..., n, with the jth region extending z_{j-1} and z_j and having thickness a_j. The two external regions are labelled 0 and $n+1$ and extend from $z_{-1} = -\infty$ to $z_0 = 0$ and from $z_n = a$ to $z_{n+1} = +\infty$. The electron beam travels either along the z-axis (normal incidence) or the x-axis (parallel incidence).

The dielectric theory of electron energy loss requires us to calculate the electric field at the position of the incoming electron due to the polarization induced in the stratified slab. In the non-retarded limit, this involves solving Poisson's equation, subject to the usual boundary conditions at interfaces, surfaces and infinity. The effects of anisotropy are dealt with by writing Poisson's equation for the potential in the jth region in the form

$$\sum_{ik} \epsilon_j^{ik}(\omega) \frac{\partial}{\partial x_i} \frac{\partial}{\partial x_k} \phi_j(\boldsymbol{r}, \omega) = -\rho_{\text{ext}}(\boldsymbol{r}, \omega)/\varepsilon_0 \tag{1}$$

where $\epsilon_j^{ik}(\omega)$ is the symmetric local dielectric tensor of the jth region. Taking the Fourier transform of (1) with respect to x and y then gives

$$\frac{\mathrm{d}^2}{\mathrm{d}z^2}\phi_j + 2\mathrm{i}\ell_j \frac{\mathrm{d}}{\mathrm{d}z}\phi_j - m_j^2 \phi_j = -\frac{\rho_{\text{ext}}(k_x, k_y, z, \omega)}{\varepsilon_0 \epsilon_j^{33}(\omega)} \tag{2}$$

where

$$m_j^2 = \left(\epsilon_j^{11} k_x^2 + 2\epsilon_j^{12} k_x k_y + \epsilon_j^{22} k_y^2\right)/\epsilon_j^{33} \tag{3}$$

$$\ell_j = \left(\epsilon_j^{13} k_x + \epsilon_j^{23} k_y\right)/\epsilon_j^{33}. \tag{4}$$

This paper solves (2) and the associated boundary conditions by using a transfer matrix recurrence relation to link the potentials in any two neighbouring regions. We then derive closed-form solutions for the potential and hence predict the energy-loss spectrum. Section 2 carries out the calculations for normal incidence, while section 3 is concerned with parallel incidence. Section 4 illustrates some consequences of our theory by performing numerical calculations for a single graphite–vacuum surface, a graphite slab surrounded by a vacuum and a graphite layer on a diamond substrate. Finally, section 5 summarizes our results and provides an outlook to future work. So far as possible, we will adopt the notation of papers I and II, including the use of square brackets to denote dispersion brackets (see [12]). It is only possible to give an outline of our methods here; readers interested in the algebraic details can find full proofs in [14] and [15].

2. Normal incidence

2.1. *Transfer matrix recurrence relation*

Suppose that the beam travels in the z-direction, normal to the interfaces of the multilayered anisotropic slab. Then a particle in the beam of charge Q and speed v has the Fourier-transformed charge density

$$\rho_{\text{ext}}(k_x, k_y, z, \omega) = \frac{Q\mathrm{e}^{\mathrm{i}\omega z/v}}{v}.$$

In order to describe the solution of (2) for this charge density, it is convenient to introduce wavevector-like variables κ_j, q_j^σ and p_j, defined by

$$\kappa_j = \sqrt{m_j^2 - \ell_j^2} \tag{5}$$

$$q_j^\sigma = \sigma\kappa_j - \mathrm{i}\ell_j \tag{6}$$

$$p_j = \sqrt{\kappa_j^2 + \omega_j^2/v^2} = \sqrt{m_j^2 + 2\omega\ell_j/v + \omega^2/v^2} \tag{7}$$

where all square roots are taken with positive real parts, $\sigma = \pm$ and

$$\omega_j = \omega + \ell_j v. \tag{8}$$

The solution to (2) can then be expressed as

$$\phi_j(k_x, k_y, z, \omega) = \sum_{\sigma=\pm} A_j^\sigma \mathrm{e}^{q_j^\sigma z} + \frac{Q\mathrm{e}^{\mathrm{i}\omega z/v}}{\varepsilon_0 v \epsilon_j^{33} p_j^2} \tag{9}$$

where the coefficients A_j^σ depend on k_x, k_y and ω. The boundary conditions at infinity require two of the coefficients to vanish, so there remain $2n+2$ undetermined coefficients which can be found from the boundary conditions at the $n+1$ interfaces. As in paper I, we recast the boundary conditions in terms of a transfer matrix recurrence relation. In order to express this recurrence relation in the simplest possible form we rescale the coefficients as follows:

$$\alpha_j^\sigma = \frac{\varepsilon_0 v}{Q} A_j^\sigma \mathrm{e}^{(q_j^\sigma - \mathrm{i}\omega/v)z_{j-1}} \qquad \text{with } \alpha_0^\sigma = \frac{\varepsilon_0 v}{Q} A_0^\sigma \tag{10}$$

and then define the **coefficient vector** for the jth layer

$$\boldsymbol{\alpha}_j = \begin{pmatrix} \alpha_j^+ \\ \alpha_j^- \end{pmatrix}.$$

We introduce the source terms

$$S_{ji}^\sigma = \sigma\kappa_i \epsilon_i^{33} \left(\frac{1}{\epsilon_j^{33} p_j^2} - \frac{1}{\epsilon_i^{33} p_i^2} \right) + \frac{\mathrm{i}}{v} \left(\frac{\omega_j}{p_j^2} - \frac{\omega_i}{p_i^2} \right) \tag{11}$$

and define **source vector** for the jth layer

$$\boldsymbol{S}_j = \begin{pmatrix} S_{j,j+1}^+ \\ -S_{j,j+1}^- \end{pmatrix}.$$

We also introduce the variables

$$h_{ji}^\sigma = \epsilon_j^{33}\kappa_j + \sigma\epsilon_i^{33}\kappa_i \tag{12}$$

and the exponential factors

$$f_j = \mathrm{e}^{\kappa_j a_j} \qquad \text{with } f_0 = f_{n+1} = 1 \tag{13}$$

$$b_j^\sigma = \mathrm{e}^{\mathrm{i}\sigma\omega_j a_j/v} \qquad \text{with } b_0^\sigma = b_{n+1}^\sigma = 1. \tag{14}$$

The boundary conditions at the interface between jth and $(j+1)$th regions then lead to the simple recurrence relation

$$\boxed{h_{j+1,j+1}^+ \boldsymbol{\alpha}_{j+1} = \frac{1}{f_j b_j^+} \boldsymbol{\tau}^{(j+1,j)} \boldsymbol{\alpha}_j + \boldsymbol{S}_j} \tag{15}$$

where the **transfer matrix** is given by

$$\boldsymbol{\tau}^{(j+1,j)} = \begin{pmatrix} h_{j+1,j}^+ f_j^2 & h_{j+1,j}^- \\ h_{j+1,j}^- f_j^2 & h_{j+1,j}^+ \end{pmatrix}. \tag{16}$$

This recurrence relation has the same form as that obtained for normal incidence on isotropic multilayers (paper I, equation (10)). Differences lie beneath the surface, though, because the terms h_{ji}^σ, S_{ji}^σ, b_j^σ and f_j defined above are more complicated than the corresponding quantities for the isotropic case. In spite of these differences, have been able to adapt the

arguments given in paper I, to obtain the following general formula for the coefficients of the potential in the jth region of an n-layered anisotropic slab:

$$\alpha_j = \frac{1}{[C_{n0}]}\left\{\sum_{k=0}^{j-1}\psi^-_{k+1,j-1}\left[X^-_{k0}\right]M_{nj} - f_j b_j^+ \sum_{k=j}^{n}\psi^+_{j+1,k}\left[Y^+_{kn}\right]N_{j-1,0}\right\}. \tag{17}$$

This is formally identical to our expression for the coefficients of the Hertz vector in the isotropic case (paper I, equation (16)). Moreover, the quantities $[C_{n0}]$, $[X^-_{k0}]$, $[Y^+_{kn}]$, M_{nj}, $N_{j-1,0}$ and ψ^σ_{ij} in (17) all have similar definitions (in terms of h^σ_{ji}, S^σ_{ji} and f_j) to the corresponding quantities of paper I. For ease of reference we restate these definitions here, but rely on paper I for more detailed descriptions. In brief, we define the monotonically ordered products:

$$C_{ji} = \prod_{k=i}^{j} h^+_{k+1,k} f_k^2 = \prod_{k=i}^{j} f_k^2 h^+_{k,k+1}$$

$$D_{ji} = C_{j,i+1}h^-_{i+1,i} \qquad E_{ji} = h^-_{j+1,j} f_j^2 C_{j-1,i}$$
$$X^\sigma_{ji} = S^\sigma_{j+1,j} f_j^2 C_{j-1,i} \qquad Y^\sigma_{ij} = S^\sigma_{i,i+1} C_{j,i+1}$$

with initial values determined by $C_{i,i+1} = 1$ and $C_{i,i+2} = 0$.

Square brackets are used to indicate **dispersion brackets** of these ordered products—i.e. the sum of all non-overlapping contractions (including the term with no contractions). Each **contraction** is defined by choosing two factors with $\pm$ superscripts, reversing the signs of these superscripts and ignoring all the f^2-factors between them. This means, for example, that

$$[C_{21}] = [h^+_{32} f_2^2 h^+_{21} f_1^2] = h^+_{32} f_2^2 h^+_{21} f_1^2 + h^-_{32} h^-_{21} f_1^2.$$

Finally, we introduce the vectors

$$M_{ji} = \begin{pmatrix} -[D_{ji}] \\ [C_{ji}] \end{pmatrix} \qquad \text{and} \qquad N_{ji} = \begin{pmatrix} [C_{ji}] \\ [E_{ji}] \end{pmatrix}$$

and take

$$\psi^\sigma_{ij} = \prod_{k=i}^{j} h^+_{kk} f_k b^\sigma_k \qquad \text{with } \psi^\sigma_{i,i-1} = 1.$$

However, we emphasize again that the similarity between these equations and those of paper I is incomplete; the anisotropy of the present problem is embedded in the definitions of S^σ_{ji}, h^σ_{ji}, f_j and b^σ_j, given by equations (11), (12), (13) and (14).

2.2. *Dispersion relation and energy-loss probability*

The dispersion relation can be found either directly from (15) or from (17). For an n-layered anisotropic slab, we obtain

$$\boxed{[C_{n0}] = 0} \tag{18}$$

which is directly analogous to equation (15) of paper I.

In order to find the semiclassical energy-loss spectrum we adopt a familiar strategy. The energy lost by an electron as it moves from $z = -\infty$ to $z = +\infty$ is calculated from the solution for the potential (equations (9), (10) and (17)). The semiclassical energy-loss spectrum is then obtained by interpreting the energy loss in terms of the exchange of

individual quanta. Proceeding as in paper I, but allowing for a more complicated dependence on k_x and k_y, the energy loss is written as

$$W = \int_0^\infty \mathrm{d}(\hbar\omega)\,\hbar\omega \int_{-\infty}^{\infty} \mathrm{d}k_x \int_{-\infty}^{\infty} \mathrm{d}k_y \,\frac{\mathrm{d}^3 P}{\mathrm{d}(\hbar\omega)\,\mathrm{d}k_x\,\mathrm{d}k_y} \tag{19}$$

and

$$\frac{\mathrm{d}^3 P}{\mathrm{d}(\hbar\omega)\,\mathrm{d}k_x\,\mathrm{d}k_y} = \frac{Q^2}{4\pi^3\varepsilon_0\hbar^2 v^2}\mathrm{Im}(\chi_{\mathrm{bulk}} + \chi_{\mathrm{bdy}}), \tag{20}$$

where χ_{bulk} represents the bulk contribution and χ_{bdy} describes the modifications due to surfaces and interfaces. The algebraic task of reducing the answer to a manageable form is harder than in the isotropic case, requiring a new calculation with several extra stages of proof [14, 15]. Nevertheless, we have been able to establish that

$$\boxed{\chi_{\mathrm{bulk}} = -\sum_{k=1}^{n} \frac{a_k}{\epsilon_k^{33} p_k^2}} \tag{21}$$

and

$$\boxed{\chi_{\mathrm{bdy}} = -\frac{1}{[C_{n0}]} \sum_{k=0}^{n}\sum_{j=k}^{n}\sum_{\sigma=\pm} z_{kj}\,\psi^{\sigma}_{k+1,j}\,[X^{\sigma}_{k0}]\,[Y^{\sigma}_{jn}]} \tag{22}$$

where $z_{kj} = 1 - \frac{1}{2}\delta_{kj}$.

As expected, the bulk contribution is a sum over layers, with the jth layer contributing an amount equal to its thickness times the energy loss per unit length in an infinite anisotropic medium with dielectric tensor $\epsilon_j^{ik}(\omega)$ (see [7]). The boundary contribution can be interpreted as a sum of couplings between pairs of interfaces. Although more complicated than χ_{bulk}, it is still remarkably simple, bearing in mind the complexity of the problem.

Equations (21) and (22) are our main theoretical results for normal incidence on anisotropic multilayers. They provide a natural extension of our previous work on isotropic multilayers and it is easy to show that their isotropic limits are the same as the non-retarded limits of equations (18) and (19)) in paper I. It is also worth noting that our final results are unchanged by the transformation $\kappa_j \to -\kappa_j$, for any $1 \leqslant j \leqslant n$. This means that the choice of square root in (5) is immaterial within the slab.

For a single anisotropic slab, the above equations simplify to

$$\chi^{(1)}_{\mathrm{bulk}} + \chi^{(1)}_{\mathrm{bdy}} = -\frac{a_1}{\epsilon_1^{33} p_1^2} - \frac{1}{[C_{n0}]} \sum_{\sigma=\pm} S^{\sigma}_{10}\left([Y^{\sigma}_{01}] + \psi^{\sigma}_{11} S^{\sigma}_{12}\right) \tag{23}$$

which is a result that will be applied to graphite slabs in section 4.

3. Parallel incidence

This section derives energy loss formulae for an electron that travels parallel to the interfaces of an anisotropic slab. We suppose that the electron travels in the mth region, parallel to the x-axis, with $y = 0$ and $z = z_{\mathrm{b}}$. Primes are used to distinguish sub-regions on either side of the beam: m' lies between z_{m-1} and z_{b}, while m'' lies between z_b and z_m.

3.1. Transfer matrix recurrence relation

A particle in the beam of charge Q and speed v has the Fourier-transformed charge density

$$\rho(k_x, k_y, z, \omega) = 2\pi Q\,\delta(\omega - k_x v)\,\delta(z - z_b)$$

Away from the beam level, $z = z_b$, we write the Fourier-transformed potential in region j as

$$\phi_j(k_x, k_y, z, \omega) = \hat{\phi}_j\,\delta(\omega - k_x v).$$

Then equation (2) is solved by taking

$$\hat{\phi}_j = \sum_{\sigma=\pm} B_j^{\sigma} e^{q_j^{\sigma} z} \tag{24}$$

where the coefficients B_j^{σ} are found by supplementing the usual boundary conditions at the $n + 1$ interfaces with two conditions at $z = z_b$:

$$\hat{\phi}_{m''}\Big|_{z_b^+} - \hat{\phi}_{m'}\Big|_{z_b^-} = 0 \tag{25}$$

and

$$\frac{d\hat{\phi}_{m''}}{dz}\bigg|_{z_b^+} - \frac{d\hat{\phi}_{m'}}{dz}\bigg|_{z_b^-} = 2\kappa_m\lambda_m \qquad \text{where } \lambda_m = -\frac{\pi Q}{\varepsilon_0 \epsilon_m^{33} \kappa_m}. \tag{26}$$

As in the calculation for normal incidence, the boundary conditions are expressed in terms of a transfer matrix recurrence relation. In order to write this recurrence relation in the simplest possible form we rescale the coefficients as follows:

$$\beta_j^{\sigma} = B_j^{\sigma} e^{q_j^{\sigma} z_{j-1}}/\lambda_m \qquad \text{with } \beta_0^{\sigma} = B_0^{\sigma}/\lambda_m \tag{27}$$

and introduce the **coefficient vector** for the jth layer

$$\beta_j = \begin{pmatrix} \beta_j^+ \\ \beta_j^- \end{pmatrix}.$$

We also introduce the **source vector**†

$$G_m = \begin{pmatrix} 1/g_m^+ \\ -1/g_m^- \end{pmatrix}$$

where

$$g_m^{\sigma} = e^{q_m^{\sigma}(z_b - z_{m-1})} \qquad \text{with } g_0^{\sigma} = e^{q_0^{\sigma} z_b}.$$

The boundary conditions at the interface between the jth and $(j + 1)$th regions, supplemented with conditions equations (25) and (26), then yield the recurrence relation

$$\boxed{\beta_{j+1} = \mathbf{T}^{(j+1,j)}\left(\beta_j + \delta_{jm'} G_m\right)} \tag{28}$$

where

$$\mathbf{T}^{(m'',m')} = \mathbf{I}$$

$$\mathbf{T}^{(j+1,j)} = \frac{e^{q_j^- a_j}}{h_{j+1,j+1}^+} \tau^{(j+1,j)} = \frac{1}{h_{j+1,j+1}^+ f_j \mu_j} \tau^{(j+1,j)} \qquad \text{for } j \neq m'$$

and

$$\mu_j = e^{i\ell_j a_j}.$$

† Care is needed here because, in the anisotropic case, $g_i^+ \neq g_i^-$.

This recurrence relation can be solved to find the coefficient vector in any given layer. We define

$$\rho_{ij} = \prod_{k=i}^{j} h_{kk}^{+} f_k \qquad \lambda_{ij} = \prod_{k=i}^{j} \mu_k$$

$$\gamma_{ji}^{\sigma} = \left[C_{ji}\right] / g_i^{+} + \sigma \left[D_{ji}\right] / g_i^{-} \qquad \zeta_{ji}^{\sigma} = \left[C_{ji}\right] g_{j+1}^{+} + \sigma \left[E_{ji}\right] g_{j+1}^{-}.$$

Then, using the boundary conditions at infinity to find the coefficients in external region 0, and applying the recurrence relation from region 0 to any region j, we obtain

$$\beta_j = -\frac{\kappa_m \epsilon_m^{33}}{\kappa_j \epsilon_j^{33}} \rho_{j,m-1} \lambda_{j,m-1} \frac{\gamma_{nm}^{-}}{\left[C_{n0}\right]} N_{j-1,0} \qquad \text{for } j \leqslant m' \tag{29}$$

and

$$\beta_j = -\frac{\rho_{m,j-1}}{\lambda_{m,j-1}} \frac{\zeta_{m-1,0}^{+}}{g_m^{+} g_m^{-}} \frac{1}{\left[C_{n0}\right]} M_{nj} \qquad \text{for } j \geqslant m''. \tag{30}$$

In particular, in the beam region itself,

$$\beta_{m'} = -\frac{\gamma_{nm}^{-}}{\left[C_{n0}\right]} N_{m-1,0} \tag{31}$$

and

$$\beta_{m''} = -\frac{\zeta_{m-1,0}^{+}}{g_m^{+} g_m^{-}} \frac{1}{\left[C_{n0}\right]} M_{nm}. \tag{32}$$

The Fourier-transformed potential in the beam region then follows from equations (24) and (27) and can be used to find the work done by the beam and hence the semiclassical energy-loss spectrum.

3.2. Dispersion relation and energy-loss probability

The dispersion relation, derived from equations (28), (29), (30), (31) or (32), takes the same form as for normal incidence ((18)). This is unlike our previous findings in paper II, where additional TE modes were found in parallel incidence which were not excited by normal incidence. These modes do not appear in the present calculation because we are working in the non-retarded limit.

To predict the energy-loss spectrum we calculate the work done on the incoming electron by the electric field induced in its polarized surroundings. The work done on the beam per unit path length can be expressed as

$$\frac{\mathrm{d}W}{\mathrm{d}x} = \int_0^{\infty} \mathrm{d}(\hbar\omega)\, \hbar\omega \int_{-\infty}^{\infty} \mathrm{d}k_y \frac{\mathrm{d}^3 P}{\mathrm{d}(\hbar\omega)\, \mathrm{d}k_y\, \mathrm{d}x} \tag{33}$$

where

$$\frac{\mathrm{d}^3 P}{\mathrm{d}(\hbar\omega)\, \mathrm{d}k_y\, \mathrm{d}x} = \frac{Q^2}{4\pi^2 \varepsilon_0 \hbar^2 v^2} \mathrm{Im}\left\{\chi_m^{(n)}\right\}_{k_x \to \omega/v} \tag{34}$$

and

$$\chi_m^{(n)} = \frac{1}{\epsilon_m^{33} \kappa_m} \sum_{\sigma=\pm} \beta_m^{\sigma} g_m^{\sigma}. \tag{35}$$

Using our solutions for the coefficient vector in the beam region (either equation (31) or equation (32)) we finally obtain

$$\boxed{\chi_m^{(n)} = -\frac{\gamma_{nm}^{-}\zeta_{m-1,0}^{+}}{\epsilon_m^{33}\kappa_m\left[C_{n0}\right]}.} \tag{36}$$

Equation (36) is our main theoretical result for parallel incidence in or near anisotropic multilayers. It extends our previous work on isotropic multilayers and, in the isotropic limit, becomes identical to equation (21) of paper II.

Our initial purpose in carrying out these calculations was to obtain formulae for single anisotropic interfaces and slabs. With this aim in mind, we now consider some special cases, beginning with that of a bulk medium, for which the number of interfaces $(n+1)$ is equal to zero. Then, substituting $n=-1$ and $m=0$ in (36) gives

$$\chi_0^{(-1)} = -\frac{1}{\epsilon_0^{33}\kappa_0} \tag{37}$$

which is consistent with the results of [9] for energy loss in a bulk anisotropic medium.

Next, we take $n=0$, corresponding to single interface at $z=0$. With the beam in region 0, we obtain

$$\chi_0^{(0)} = -\frac{1}{\epsilon_0^{33}\kappa_0}\left(1-\frac{h_{10}^{-}}{h_{10}^{+}}e^{2\kappa_0 z_b}\right) \tag{38}$$

and with the beam in region 1, we obtain

$$\chi_1^{(0)} = -\frac{1}{\epsilon_1^{33}\kappa_1}\left(1+\frac{h_{10}^{-}}{h_{10}^{+}}e^{-2\kappa_1 z_b}\right) \tag{39}$$

As expected, equations (38) and (39) transform into one another if we make the replacements $0 \leftrightarrow 1$ and $z_b \leftrightarrow -z_b$. Also, at the interface itself, $\chi_0^{(0)} = \chi_1^{(0)}$.

Finally, consider the case of a single slab. On substituting $n=1$ and $m=1$ in (36), we obtain the energy-loss function for an internal beam:

$$\chi_1^{(1)} = -\frac{1}{\epsilon_1^{33}\kappa_1\left[C_{10}\right]}\left(h_{21}^{+}e^{2\kappa_1(a_1-z_b)}-h_{21}^{-}\right)\left(h_{10}^{+}e^{2\kappa_1 z_b}+h_{10}^{-}\right) \tag{40}$$

while substituting $n=1$ and either $m=0$ or $m=2$ gives the expressions for an external beam:

$$\chi_0^{(1)} = -\frac{1}{\epsilon_0^{33}\kappa_0}\left(1-\frac{h_{21}^{+}f_1^2h_{10}^{-}+h_{21}^{-}h_{10}^{+}}{h_{21}^{+}f_1^2h_{10}^{+}+h_{21}^{-}h_{10}^{-}}e^{2\kappa_0 z_b}\right) \tag{41}$$

$$\chi_2^{(1)} = -\frac{1}{\epsilon_2^{33}\kappa_2}\left(1+\frac{h_{21}^{-}f_1^2h_{10}^{+}+h_{21}^{+}h_{10}^{-}}{h_{21}^{+}f_1^2h_{10}^{+}+h_{21}^{-}h_{10}^{-}}e^{-2\kappa_2(z_b-a_1)}\right). \tag{42}$$

Equations (41) and (42) transform into one another if we make the replacements $0 \leftrightarrow 2$ and $z_b \leftrightarrow a_1 - z_b$. Also, (40) agrees with (41) when $z_b = 0$ and it agrees with (42) when $z_b = a_1$. In the next section, these equations will be applied to graphite slabs surrounded by vacuum and diamond.

4. Applications of the scattering formulae

This section applies the theoretical formulae derived above to energy-loss spectra of graphite, a typical uniaxial material. As this is the first analysis that includes surface and interface terms for anisotropic materials, we concentrate on the simplest geometries—a single slab, a single interface and a surface coating of graphite on diamond. We consider three different orientations, with the anisotropy axis (the c-axis) aligned along the x-, y- and z-axes. For brevity, these will be referred to as the $\hat{x}$-, $\hat{y}$- and $\hat{z}$-orientations. In all the graphs that follow, a solid line will be used for the $\hat{z}$-orientation, a dashed line for the $\hat{y}$-orientation and a dotted line for the $\hat{x}$-orientation. The dielectric tensors for these orientations are

$$\epsilon_x = \begin{pmatrix} \epsilon^{\parallel} & 0 & 0 \\ 0 & \epsilon^{\perp} & 0 \\ 0 & 0 & \epsilon^{\perp} \end{pmatrix} \qquad \epsilon_y = \begin{pmatrix} \epsilon^{\perp} & 0 & 0 \\ 0 & \epsilon^{\parallel} & 0 \\ 0 & 0 & \epsilon^{\perp} \end{pmatrix} \qquad \epsilon_z = \begin{pmatrix} \epsilon^{\perp} & 0 & 0 \\ 0 & \epsilon^{\perp} & 0 \\ 0 & 0 & \epsilon^{\parallel} \end{pmatrix}$$

where $\epsilon^{\parallel}$ is the dielectric function when the electric field is parallel to the c-axis and $\epsilon^{\perp}$ is the dielectric function when the electric field is perpendicular to the c-axis. Numerical values of these dielectric functions are taken from the *Handbook of Optical Constants of Solids II* by Palik [16].

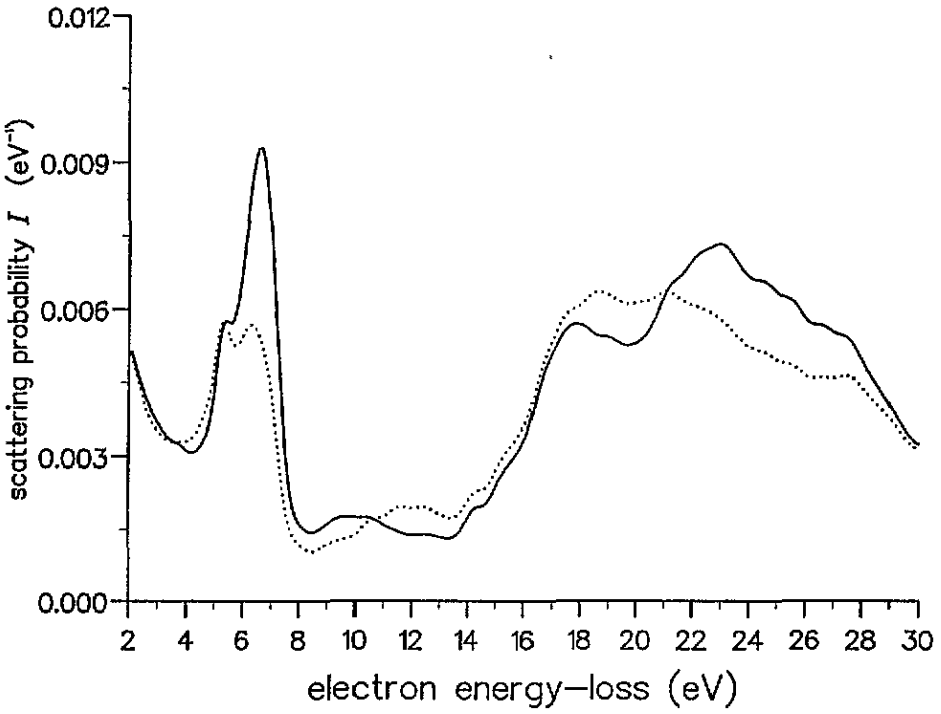

Figure 1. The scattering probability per unit energy range $I(\hbar\omega)$ for normal incidence on a single graphite slab of thickness 100 Å. The solid line corresponds the $\hat{z}$-orientation and the dotted line to the equivalent $\hat{x}$- and $\hat{y}$-orientations.

The intensity of an energy-resolved STEM image is proportional to the scattering probability per unit energy range, $I(\hbar\omega)$, which is obtained by integrating equations (20) or (34) over wavevectors. To avoid the logarithmic divergence that always accompanies bulk

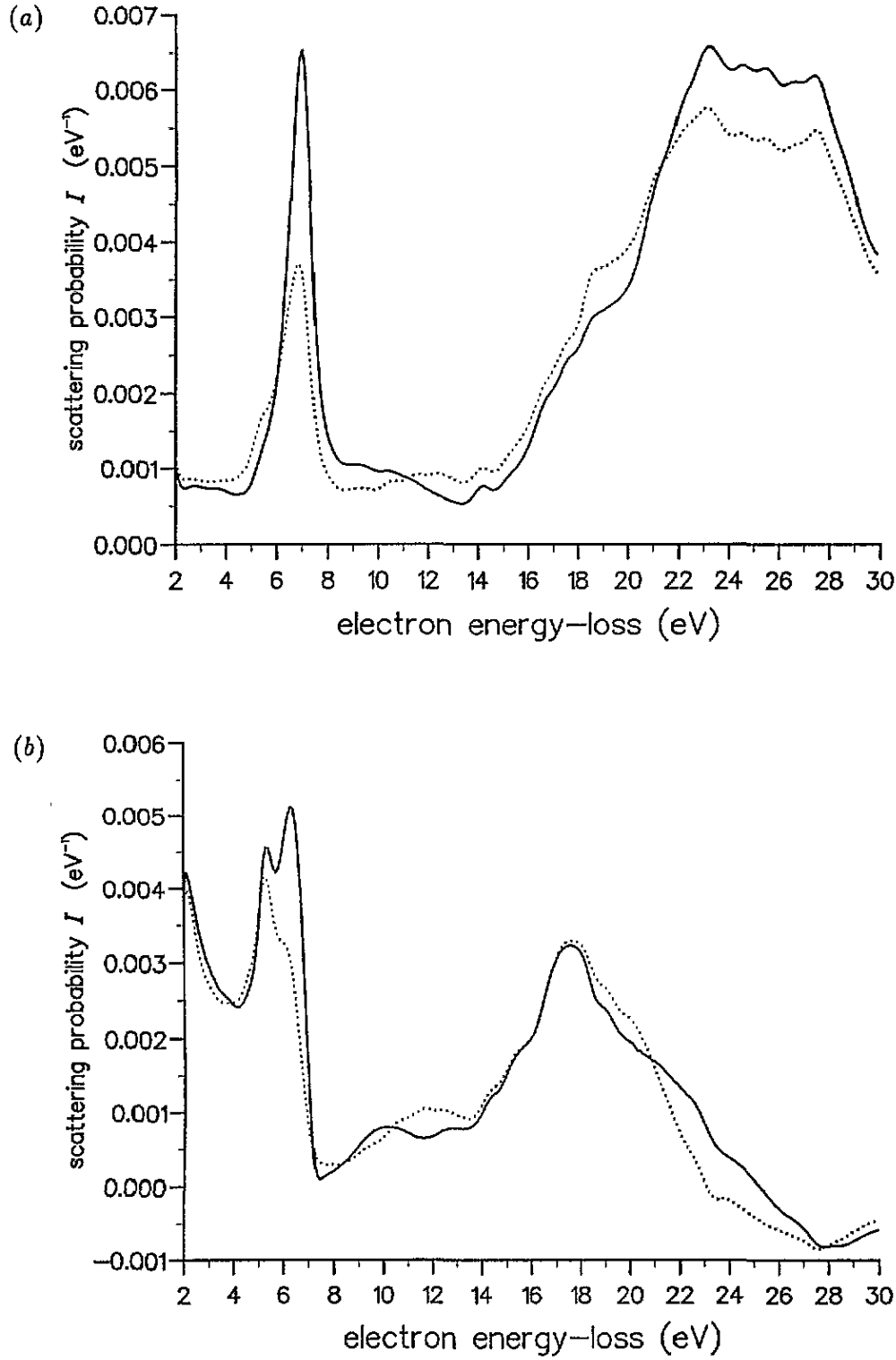

Figure 2. Contributions to the energy-loss spectra of figure 1: (*a*) bulk contributions; (*b*) surface contributions.

losses it is necessary to introduce an upper wavenumber cut-off, k_c. For normal incidence we take

$$I(\hbar\omega) = \int_{-k_c}^{k_c} \mathrm{d}k_x \int_{-\sqrt{k_c^2-k_x^2}}^{\sqrt{k_c^2-k_x^2}} \mathrm{d}k_y \, \frac{\mathrm{d}^3 P}{\mathrm{d}(\hbar\omega)\,\mathrm{d}k_x\,\mathrm{d}k_y} \tag{43}$$

and for parallel incidence

$$\frac{\mathrm{d}I(\hbar\omega)}{\mathrm{d}x} = \int_{-k_c}^{k_c} \mathrm{d}k_y \, \frac{\mathrm{d}^3 P}{\mathrm{d}(\hbar\omega)\,\mathrm{d}k_y\,\mathrm{d}x}. \tag{44}$$

In practice, k_c is often determined by the size of the objective aperture which restricts the scattering angle, so it is appropriate to impose the cut-off isotropically as in (43); in any case, $I(\hbar\omega)$ is fairly insensitive to the cut-off and (43) provides a simple and convenient choice. In the following examples the beam energy has been set at 100 keV and the cut-off wavevector has been chosen to be 15 nm^{-1} (corresponding to scattering through a maximum angle of 9 mrad).

Our first example is that of normal incidence on a single graphite slab of thickness 100 Å (figure 1). The effects of anisotropy are clearly seen in the differences between the energy-loss spectra for the $\hat{z}$-orientation (solid line) and the two equivalent $\hat{x}$- and $\hat{y}$-orientations (dotted line). The interpretation of these spectra is aided by plotting the bulk and surface contributions separately (figure 2).

In general agreement with previous work [2, 17], the bulk contributions have significant features at 5.5 eV, 7 eV, 19 eV and below 28 eV (figure 2(*a*)). The 5.5 eV shoulder and the 7 eV peak are associated with π-plasmons (strictly speaking, combinations of collective and single-particle excitations of the π-electrons). The 5.5 eV mode is excited only by momentum transfers parallel to the *c*-axis, while the 7 eV mode requires the momentum transfer to be perpendicular to the *c*-axis. The shoulder at 19 eV and the peaks below 28 eV are associated with coupled $(\sigma + \pi)$-plasmons. These modes are excited by momentum transfers that are, respectively, parallel and perpendicular to the *c*-axis. It follows from the geometry of the scattering process that the $\hat{z}$-orientation should strongly suppress the 5.5 eV and 19 eV plasmons but moderately favour the 7 eV and 28 eV plasmons. Figure 2(*a*) agrees with this prediction.

The surface contributions, shown in figure 2(*b*), are dominated by surface plasmons around 6 eV and 18 eV. The low-energy surface plasmon modes are broader and stronger for the $\hat{z}$-orientation than for the other orientations. This offsets the narrowness of the low-energy bulk mode in the $\hat{z}$-orientation and explains why the low-energy peak in figure 1 has a similar width for all orientations of the *c*-axis. The surface mode at 18 eV is not very sensitive to the direction of the *c*-axis and is evident in all the energy-loss spectra of figure 1. The $\hat{x}$-and $\hat{y}$-orientations produce slightly greater energy loss in this region because the 18 eV surface mode merges with the 19 eV bulk mode that exists for these orientations. The 18 eV surface plasmon is broad enough to modify the shape of the loss spectrum above 20 eV; the peaks are shifted to lower energies than in the bulk spectrum because the surface contribution decreases with increasing energy. Finally, note that the weak structure in the spectrum between 9 eV and 13 eV is largely due to surface contributions, but these losses are best described as background because analysis of the dispersion relation $[C_{10}] = 0$ shows that there are no self-sustaining surface plasmon modes in this range.

Our next example is that of parallel incidence near a graphite–vacuum interface. Figure 3(*a*) shows $\mathrm{d}I(\hbar\omega)/\mathrm{d}x$, the scattering probability per unit energy range per unit path length for an electron travelling in the graphite region, 15 Å away from the interface. The usual bulk modes can be identified at 5.5 eV, 7 eV, 19 eV and 27.5 eV. In the $\hat{x}$-orientation,

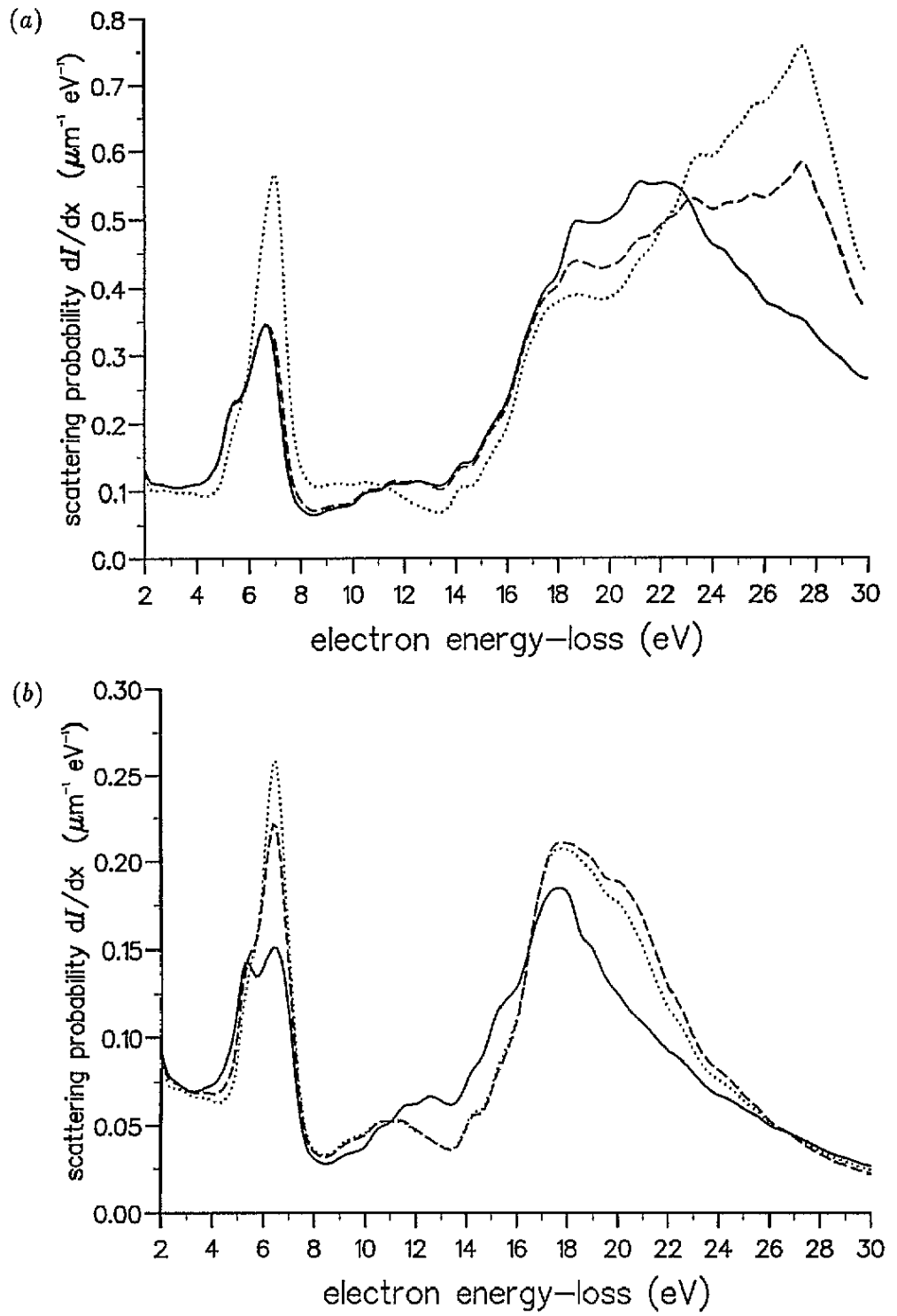

Figure 3. Scattering probability per unit energy range per unit path length, $\mathrm{d}I(\hbar\omega)/\mathrm{d}x$, for an electron, travelling parallel to, and 15 Å away from, the interface between semi-infinite graphite and vacuum regions: (*a*) electron in graphite; (*b*) electron in vacuum.

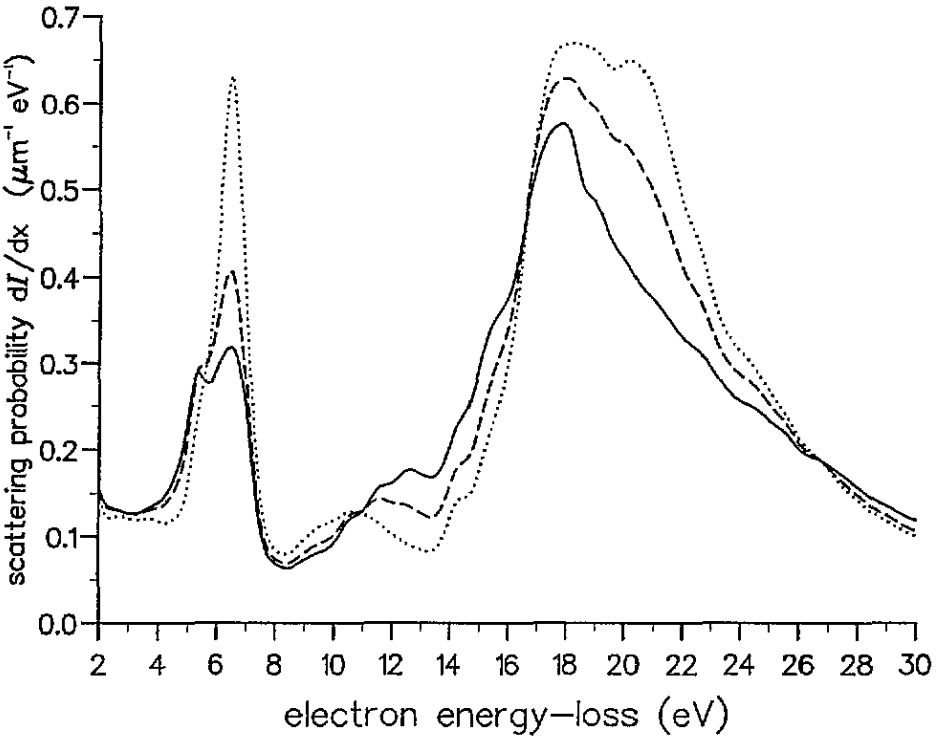

Figure 4. Scattering probability per unit energy range per unit path length, $dI(\hbar\omega)/dx$, for an electron travelling at the surface between semi-infinite vacuum and graphite regions.

the c-axis is parallel to the beam, so the 5.5 eV and 19 eV modes are strongly suppressed and the 7 eV and 27.5 eV modes moderately enhanced in this orientation. With the beam in this position (i.e. inside the graphite region) the surface contributions are much smaller than those due to the bulk, but a detailed analysis shows that they increase the effects of anisotropy for the 27.5 eV mode and a decrease them for the 5–7 eV modes.

Very different results are obtained when the beam is outside the graphite region. Figure 3(b) shows $dI(\hbar\omega)/dx$ for an electron travelling in the vacuum region, 15 Å away from the interface. This spectrum is dominated by surface effects so there are no features at 28 eV. There are significant effects due to anisotropy in the surface modes. In comparison with the $\hat{z}$-orientation, the $\hat{x}$- and $\hat{y}$-orientations produce broader modes around 18–20 eV and slightly narrower modes around 5–7 eV. Figure 4 shows the energy-loss spectrum when the beam is at the interface. This is quite similar to figure 3(b), but the 18–20 eV modes are now comparatively more pronounced, particularly in the case of the $\hat{x}$-orientation.

Our final example considers a thin graphite slab of thickness 30 Å, sandwiched between semi-infinite vacuum and diamond regions. Figure 5(a) shows the energy-loss spectrum calculated for an electron in the middle of the graphite slab. The main features of this spectrum are similar to those of figure 3(a). When the electron beam is moved to the graphite–diamond interface, the spectrum alters considerably (figure 5(b)). The modes between 28 eV and 30 eV can be interpreted as a combination of bulk graphite and bulk diamond modes. The peaks at 14 eV and 22 eV coincide with minor features in the spectrum for bulk diamond, but they also include significant contributions from the graphite–diamond interface. Separate analysis of the interface contribution reveals considerable anisotropy

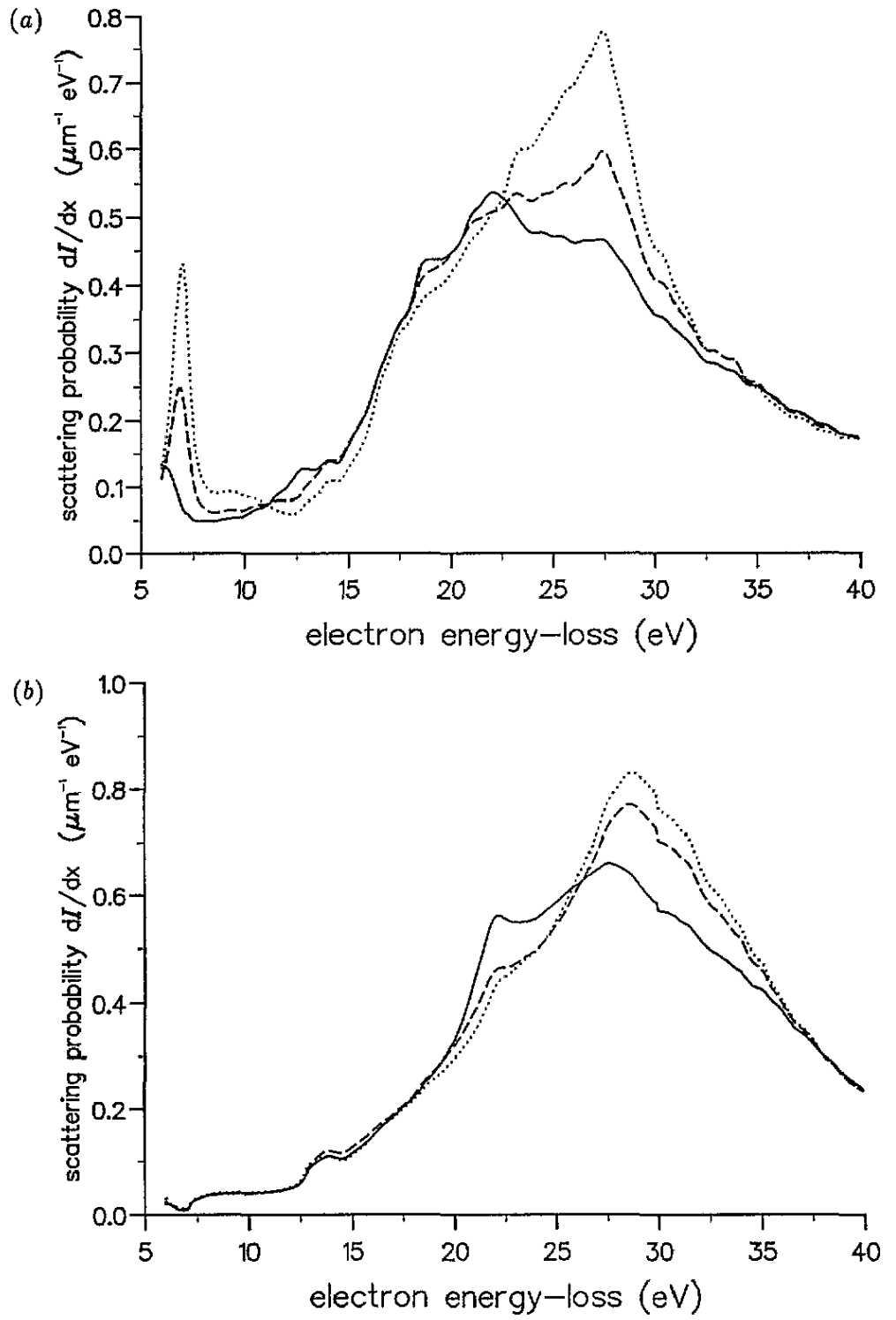

Figure 5. Scattering probability per unit energy range per unit path length, $dI(\hbar\omega)/dx$, for an electron travelling parallel to the interfaces of a diamond/graphite/vacuum sandwich structure: (*a*) electron in middle of graphite region; (*b*) electron at diamond–graphite interface.

around 22 eV, with the $\hat{z}$-orientation producing more scattering than the other orientations, leading to an enhanced 22 eV peak in the $\hat{z}$-orientation of figure 5(*b*). Between 26 eV and 36 eV the interface contributions favour the $\hat{x}$- and $\hat{y}$-orientations.

5. Conclusions

This paper has developed the programme of paper I and paper II by extending the classical dielectric theory of electron energy loss to multilayered anisotropic slabs. We have derived closed-form expressions for the dispersion relation and the energy-loss spectrum for both normal and parallel incidence and for any orientation of the anisotropy axes. The close similarity between these results and our previous findings in papers I and II supports our general belief that dispersion brackets are the natural way of expressing the solutions to multilayer problems.

Calculations on graphite have shown that anisotropic effects are important for both bulk and surface plasmons. In future, we hope to extend these calculations to include the effects of retardation. The retarded calculation is likely to be much more complicated than the classical theory presented here because it combines the difficulties of a dielectric tensor with a 4×4 transfer matrix. Nevertheless, we hope that progress will be possible in the near future.

References

[1] Hubbard J 1955 *Proc. R. Soc.* A **68** 411, 976
[2] Zeppenfeld K 1968 *Z. Phys.* **211** 391
[3] Kincaid B M, Meixner A E and Platzman P M 1978 *Phys. Rev. Lett.* **40** 1296
[4] Leapman R D, Fejes P L and Silcox J 1983 *Phys. Rev.* B **28** 2361
[5] Batson P E and Chisholm M F 1988 *Phys. Rev.* B **37** 635
[6] Nucker N, Romberg H, Xi X X, Fink J, Gegenheimer B and Zhao Z X 1989 *Phys. Rev.* B **39** 6619
[7] Raether H 1980 *Springer Tracts in Modern Physics* (Berlin: Springer)
[8] Browning N D, Yuan J and Brown L M 1991 *Ultramicroscopy* **38** 291–8
[9] Browning N D, Yuan J and Brown L M 1993 *Phil. Mag.* A **67** 261–71
[10] Ritchie R H 1957 *Phys. Rev.* **106** 874–81
[11] Howie A 1983 *Ultramicroscopy* **11** 141
[12] Bolton J P R and Chen M 1995 *J. Phys.: Condens. Matter* **7** 3373
[13] Bolton J P R and Chen M 1995 *J. Phys.: Condens. Matter* **7** 3389
[14] Chen M 1994 Applications of computer algebra to the theory of electron energy loss *PhD Thesis* Open University
[15] Bolton J P R and Chen M 1994 Dispersion brackets and electron energy loss *Open University Technical Report*
[16] Palik E D 1991 *Handbook of Optical Constants of Solids II* (Boston, MA: Academic)
[17] Fallon P J 1992 *PhD Thesis* University of Cambridge